Sea-Spike Backscatter from a Steepening Wave

Dennis Holliday, Lester L. DeRaad, Jr., and Gaetan J. St-Cyr

***Abstract*— H-pol and V-pol backscatter cross sections at incidence angles of 85°, 60°, and 40° are computed at X-band for two temporal sequences of simulated sea waves, one with a wavelength of 1 m and the other with a 2.3-m wavelength, that are steepening as they undergo breaking. At an incidence angle of 85° (5° grazing) H-pol and V-pol backscatter from these waves are shown to have the characteristics of a sea spike. At a 60° incidence angle only the 1-m sequence produces a sea spike. No sea spike is seen from either sequence at 40°.**

***Index Terms*—Sea surface electromagnetic scattering.**

I. Introduction

At a low-grazing angle when the wind direction is toward the radar, high-frequency radar returns from the sea surface exhibit a number of features strikingly different from high-grazing angle backscatter. (A comprehensive review of the literature on sea clutter, including low-grazing angle data, can be found in [1].) Below about 10° grazing, sharp peaks in a temporal display of backscatter intensity (which are known as sea spikes) are often observed to have absolute cross sections in excess of 1 m^2 at 10 GHz; in some cases 10 m^2 [1, Sec. 13.17]. The change of cross section during the process of peaking can exceed 10 or sometimes 20 dB in a time of the order of 100 ms. The peaks in cross section, when measured by calibrated polarimetric radars, can have ratios of $\sigma_{\rm HH}$, the cross section for horizontally transmitted and horizontally received electric fields, to $\sigma_{\rm VV}$, its vertically polarized counterpart of 0 dB or greater. Associated with these peaks is an ambient sea surface backscatter that has a ratio of the average $\sigma_{\rm HH}$ to average $\sigma_{\rm VV}$ of between -15 dB to a few positive decibels; the ambient backscatter also has a considerably higher mean Doppler for horizontal (HH) than for vertical (VV) when the wind direction is toward the radar. None of these features has been explained quantitatively although a number of unsuccessful attempts have been made, including recent work on backscatter by wedges [2], [3].

A theoretical explanation of sea-spike phenomena, as described above, should be based on a demonstration that some temporally evolving sea wave can, in accordance with the electromagnetic equations, produce backscatter with the following characteristics [1]:

1) sea-spike behavior occurs; that is, the backscatter intensity (proportional to the square of the electric field) in a resolution cell can increase by 10 dB or more in a time of the order of 100 ms;
2) the maximum backscatter cross section at the peak of the sea spike can be the order of 1 m^2 or larger—in some cases 10 m^2;
3) the $\sigma_{\rm HH}/\sigma_{\rm VV}$ ratio at the peak of the sea spike can be 0 dB or greater.

Using previously developed methods for computing scattering from perfect and imperfect conductors [4], [5], we have obtained the above characteristics for X-band (10 GHz) backscatter from simulated sea waves that are in the deformation phase of wave breaking. A description of these results and their interpretation are the main subject of this paper.

II. Breaking Sea Waves

Wang *et al*. at the Ocean Engineering Laboratory of the University of California, Santa Barbara (UCSB), have developed a numerical wavetank (called LONGTANK) for the study of wave groups, wave-wave interactions, wave deformation, wave breaking, and other nonlinear effects [6]. Their calculations of wave shapes are consistent with tank experiments and ocean observations. Two sets of their results, Case 2.4 and 2.5, have been provided to us in the form of digitized waveforms, which will be referred to as UCSB waves, representing the evolution of 2.3-m wavelength and 1.0-m wavelength sea waves, respectively [7]. In each case the peak wave in the group, which is in the deformation phase of wave breaking, is followed for a time interval—180 ms for Case 2.4 and 190 ms for Case 2.5—beginning close to the inception of the breaking process and ending with jet initiation at the crest of the wave.

The evolution of the peak wave in Case 2.4 is shown in Fig. 1, where the waves in the group ahead of and behind the peak wave are, for simplicity, not shown; the period of the waves is $T = 1.212$ s. The wave height (measured from $z = 0$) is about 18 cm. The interval of time between the 16 Case 2.4 waves is 12 ms except for the interval between waves 2 and 3 and waves 3 and 4, which are 14 and 10 ms, respectively. As can be seen from Fig. 1, wave 1 shows some steepening, while wave 12 shows the beginning of jet formation.

Fig. 2 shows seven waves depicting the evolution of the peak wave in Case 2.5. The wave height is about 8 cm, which is close to 18 cm/2.3, thus demonstrating that Cases 2.5 and 2.4 are related by the wavelength ratio scaling factor; the period of the waves in Case 2.5 is $T = 0.801$ s. The time interval between the first five waves is 40 ms; between waves 5 and 6 and between waves 6 and 7 the time intervals are 20 and 10 ms, respectively. As can be seen from Fig. 2; wave 1 looks approximately sinusoidal, while the final wave 7, which is 190 ms later, shows incipient jet formation. Although surface tension effects are included in the LONGTANK computations that produced both Case 2.5 and Case 2.4, these effects are

Manuscript received December 13, 1996; revised August 18, 1997. This work was supported by the Department of Defense under contract DMA800-94-C-6010.

The author is with Logicon, Los Angeles, CA 90009 USA.

Publisher Item Identifier S 0018-926X(98)01039-4.

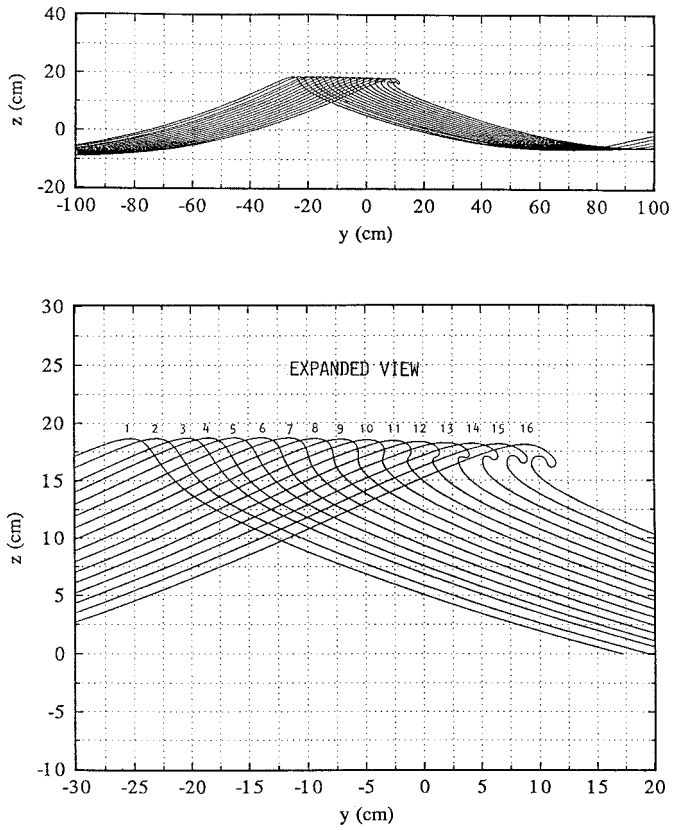

Fig. 1. UCSB Case 2.4 (2.3-m wavelength) $t/T = 33.77$ to 33.92.

largely manifested at the late stages of breaking so that the waves in Case 2.5 and in Case 2.4 evolve up to jet initiation in a scaled manner with the latter case changing at a rate about $\sqrt{2.3}$ times slower than the former.

Readers should note that both UCSB waves in this study are idealized sea waves because they are devoid of the complex smaller scale features observed on actual ocean waves.

III. Scattering Theory and Computational Method

To compute backscatter from the breaking waves described in the previous section, we use a recently developed method [5] that applies to scattering from imperfect conductors such as sea water, for which the dielectric constant is well approximated by $\epsilon = 65 + i\ 40$ at X-band (10 GHz) [8]; the permeability of sea water is unity. A brief discussion of this new method may be helpful. For the sake of brevity, only H-pol will be reviewed. For V-pol and additional details the reader is referred to Holliday *et al.* [5] .

The surface wave that produces the backscatter will be described by a height function $z = \eta(y)$, where $\widehat{y}$ is the unit vector in the negative range direction, i.e., toward the source of the incident electromagnetic field. The unit vector $\widehat{x}$ is in the azimuth direction. Since η can be a multiply-valued function of y, the path length ℓ will be a computationally simpler coordinate, and a point on the surface at ℓ will be described by a vertical position $z(\ell)$ and a horizontal position $y(\ell)$. On the surface η the magnetic and electric fields will be described by $J_{\rm H}(\ell) = \widehat{x} \cdot [\widehat{n}(\ell) \times \mathbf{B}(\ell)]$ and $L_{\rm H}(\ell) = \widehat{t}(\ell) \cdot [\widehat{n}(\ell) \times \mathbf{E}(\ell)]$; $\widehat{n}(\ell)$ and $\widehat{t}(\ell)$ are the unit normal and tangential vectors

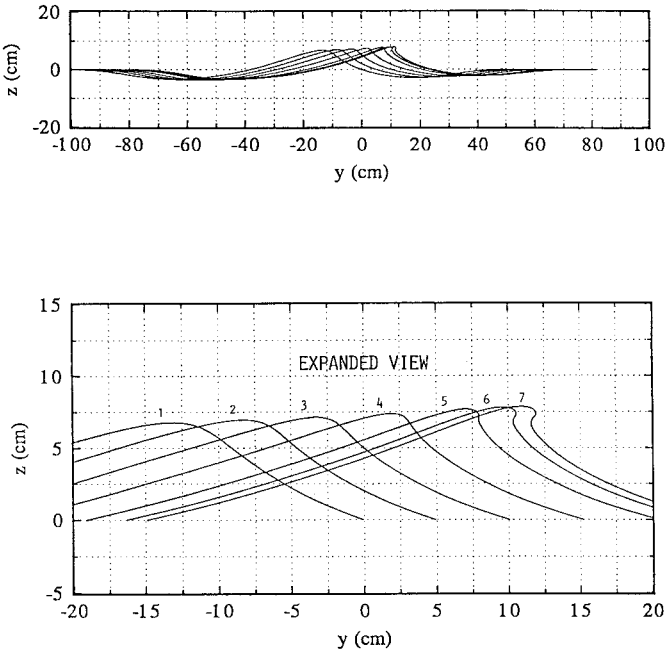

Fig. 2. UCSB Case 2.5 (1.0 m wavelength) $t/T = 58.20$ to 58.4377.

to the surface at the path length position ℓ. The functions $J_{\rm H}(\ell)$ and $L_{\rm H}(\ell)$ are obtained by solving a pair of coupled integral equations. Using these functions one can compute the asymptotic backscattered field amplitudes (in cgs units: statvolts/cm for electric fields and Gauss for magnetic fields) for H-pol plane wave incident radiation

$$\widehat{x} \cdot \mathbf{E}_S = \frac{i}{2} \frac{e^{i(\kappa r + \pi/4)}}{\sqrt{2\pi\kappa r}} \mathcal{B}_{\rm H} \tag{1}$$

where

$$\begin{aligned} \mathcal{B}_{\rm H} = \kappa \int_{-\infty}^{+\infty} \Big\{ & [J_{\rm H}(\ell') - \widehat{n}(\ell') \cdot \widehat{\kappa} L_{\rm H}(\ell')] e^{-i\phi(\ell')} \\ & - \left[\sqrt{\epsilon - \sin^2\theta} - \cos\theta\right] \\ & \cdot L_0 \frac{dy(\ell')}{d\ell'}\ e^{-i2\kappa \sin\theta y(\ell')} \Big\}\ d\ell'. \end{aligned} \tag{2}$$

In (1) and (2), the following definitions apply:

κ	wavenumber of the incident electromagnetic field;
θ	incidence angle of the incident electromagnetic field (and reflection angle of the backscattered electromagnetic field);
r	$\sqrt{y^2 + z^2}$;
$\widehat{\kappa}$	$(0,\ \sin\theta,\ \cos\theta)$;
$\phi(\ell)$	$\kappa[\sin\theta y(\ell) + \cos\theta z(\ell)]$;
L_0	$2\cos\theta / \left[\cos\theta + \sqrt{\epsilon - \sin^2\theta}\right]$.

Actual ocean waves will have limited azimuthal extent. However, if the extent ℓ_x is large compared to a wavelength $\kappa\ell_x \gg 1$ then the azimuthally homogeneous calculation can be used to calculate an approximate cross section

$$\sigma_{\rm HH} \cong \frac{\ell_x^2}{4\pi} \left|\mathcal{B}_{\rm H}\right|^2 \tag{3}$$

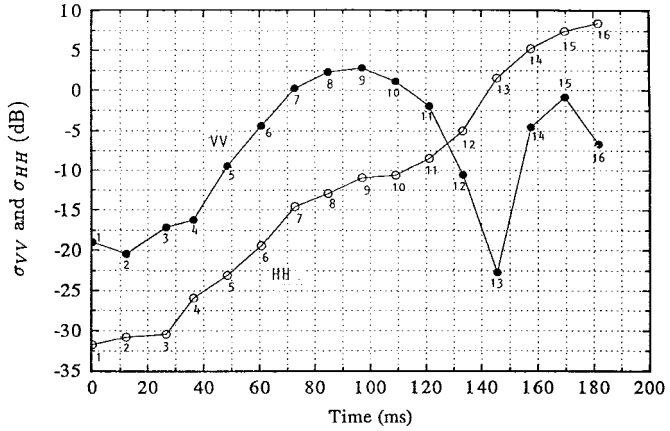

Fig. 3. σ_{HH} and σ_{VV} for Case 2.4 (16 waves) at $\theta = 85°$.

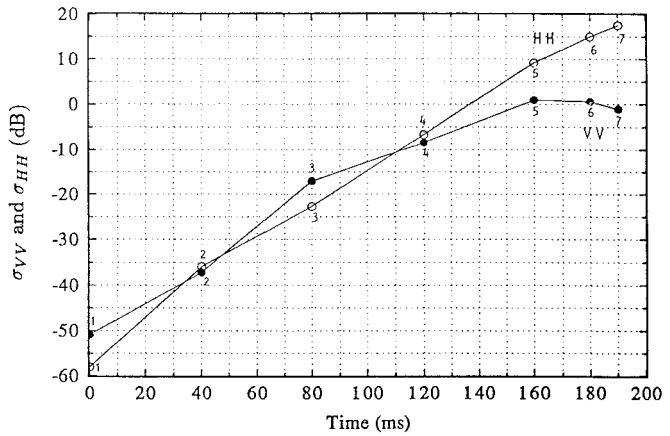

Fig. 4. σ_{HH} and σ_{VV} for Case 2.5 (7 waves) at $\theta = 85°$.

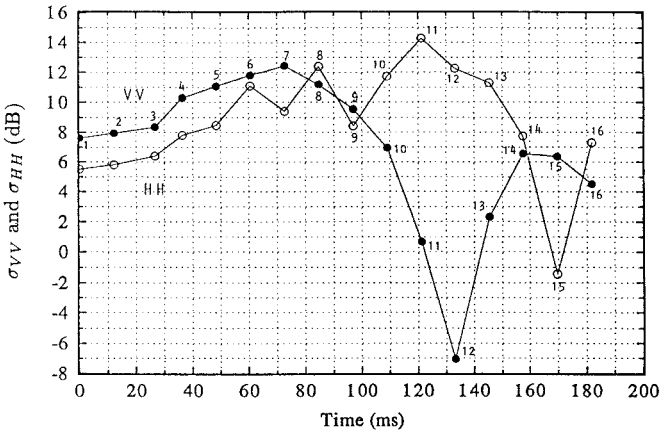

Fig. 5. σ_{HH} and σ_{VV} for Case 2.4 (16 waves) at $\theta = 60°$.

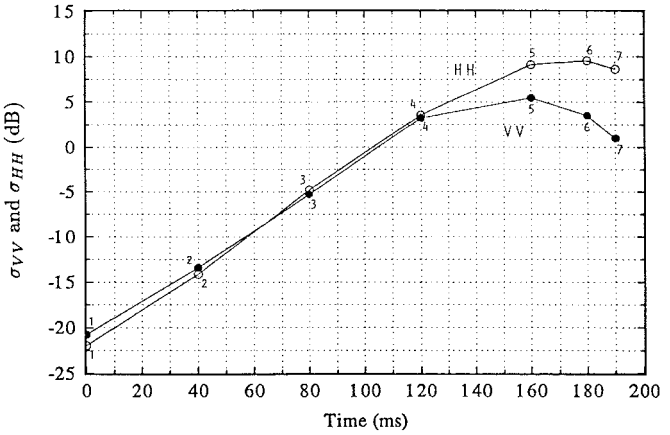

Fig. 6. σ_{HH} and σ_{VV} for Case 2.5 (7 waves) at $\theta = 60°$.

and

$$\sigma_{\mathrm{VV}} \cong \frac{\ell_x^2}{4\pi}\left|\mathcal{B}_{\mathrm{V}}\right|^2 \tag{4}$$

where $\mathcal{B}_{\mathrm{V}}$ is the V-pol scattering amplitude in analogy to $\mathcal{B}_{\mathrm{H}}$ (2). This approximation produces the azimuthal length squared, i.e., ℓ_x^2, dependence of backscatter cross section from a number of single objects [9].

IV. Results

Using the new method for low-grazing angle scattering from imperfect conductors [5], which was discussed in the previous section, we have computed the backscatter cross sections σ_{HH} and σ_{VV} at $\theta = 85°$ (5° grazing), $\theta = 60°$ (30° grazing), and $\theta = 40°$ (50° grazing) for each wave in Fig. 1 (16 waves) and Fig. 2 (7 waves). The wave that ultimately produces an incipient jet has been isolated from the complete wave train produced by LONGTANK by means of a "cosine-on-a-pedestal" weighting ahead of and behind this wave [5, Sec. 4]. In particular, the region that contained the peak wave and the two nearest troughs was retained. In addition, 50 cm of surface on either side of this region was smoothly brought to the mean surface level. The values for σ_{HH} and σ_{VV} are shown as functions of time in Figs. 3–8; a reference value of $\ell_x = 1$ m is used in these calculations and, according to (3) and (4), the cross sections are proportional to ℓ_x^2.

For Case 2.4, as shown in Fig. 3, the H-pol cross section σ_{HH} at $\theta = 85°$ increases by about 20 dB in the 100 ms preceding incipient jet formation (wave 12 or wave 13); 0 dB is a cross section of 1 m^2. The V-pol cross section σ_{VV} varies more rapidly than σ_{HH} in this time interval and is not a monatomic function of time as is σ_{HH}. A striking dip in σ_{VV} is observed for wave 13, which is likely due to destructive interference phenomena. Ratios of σ_{HH} to σ_{VV} of between 0 and 20 dB are seen for waves 12–16. For $\ell_x = 1$ m the peak value of σ_{HH} is about 7 m^2 (wave 16), which would decrease to 0.6 m^2 for $\ell_x = 0.3$ m.

Fig. 4 shows that Case 2.5, which has a wave height of about 8 cm, produces a σ_{HH} at $\theta = 85°$ that increases by about 35 dB in the 100 ms prior to incipient jet formation, during which time σ_{VV} increases by about 21 dB. There is no dip in σ_{VV} similar to what is seen in Fig. 3. Ratios of σ_{HH} to σ_{VV} of between 0 and 20 dB are seen for waves 4–7. The peak value of σ_{HH} is about 60 m^2 (wave 7) for $\ell_x = 1$ m, which would decrease to 5.4 m^2 for $\ell_x = 0.3$ m.

Figs. 3 and 4 demonstrate that X-band backscatter from each series of waves, Case 2.4 (2.3 m) and Case 2.5 (1 m), fits the description of a sea spike in Section 1, which was based on the review of experimental data by Wetzel [1]. A

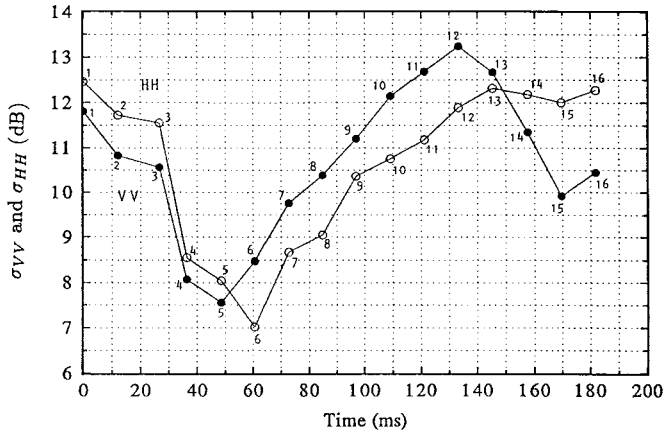

Fig. 7. σ_{HH} and σ_{VV} for Case 2.4 (16 waves) at $\theta = 40°$.

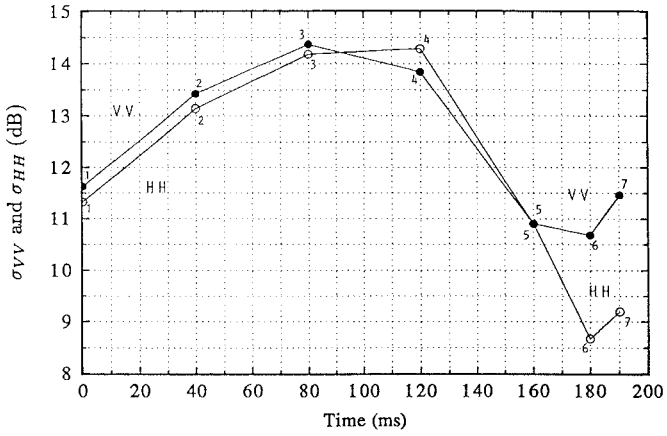

Fig. 8. σ_{HH} and σ_{VV} for Case 2.5 (7 waves) at $\theta = 40°$.

very important conclusion from a comparison of Fig. 3 with Fig. 4 is that (for the same ℓ_x) a *smaller amplitude steepening sea wave can produce a larger sea spike with a faster rise time than a steepening sea wave with a significantly greater height*. Sea spikes that are observed in ocean backscatter are not necessarily produced by the waves with the largest heights.

Fig. 4 also shows that a sea spike can be produced by a steepening wave *before* a noticeable jet begins to form at the crest of the wave. This result is consistent with the many observations of sea-spike behavior in the absence of noticeable wave breaking.

Very much slower variations in both σ_{HH} and σ_{VV} are observed at $\theta = 60°$ than at $\theta = 85°$. Figs. 5 and 6 show the $\theta = 60°$ results for Cases 2.4 and 2.5, respectively. For the whole series of 16 waves in Case 2.4, σ_{HH}, except for the dip at wave 15, varies only ± 4 dB about 15 m^2. Note the dip in σ_{VV} for wave 12, which is similar to the dip for wave 13 in Fig. 3. Fig. 6 shows that σ_{HH} and σ_{VV} for Case 2.5 at $\theta = 60°$ increases at about half the decibel rate as the cross sections at $\theta = 85°$. In fact, there is a considerable similarity between Figs. 4 and 6 if the dB scale at $\theta = 85°$ is halved. The $\theta = 60°$ results show that Case 2.5 (1-m wavelength, 8-cm crest height) does produce backscatter that could be characterized as a sea spike, but that Case 2.4 does not.

TABLE I
CHANGE IN BACKSCATTER CROSS SECTION FOR CASE 2.4 FROM WAVE 3 TO WAVE 12 (110 ms)

	$\theta = 85°$	$\theta = 60°$	$\theta = 40°$
dB change in σ_{HH}	+26	+6	+0.3
dB change in σ_{VV}	+7	−15	+3

TABLE II
CHANGE IN BACKSCATTER CROSS SECTION FOR CASE 2.5 FROM WAVE 3 TO WAVE 7 (110 ms)

	$\theta = 85°$	$\theta = 60°$	$\theta = 40°$
dB change in σ_{HH}	+41	+13	−5
dB change in σ_{VV}	+16	+6	−3

As shown in Figs. 7 and 8, even slower variations in cross section are observed at $\theta = 40°$ than at $\theta = 60°$. At $\theta = 40°$, σ_{HH} and σ_{VV} are essentially identical with variations confined to ± 3 dB about a mean value, which is 10 m^2 for Case 2.4 and 14 m^2 for Case 2.5. No sea spikes are seen in Figs. 7 and 8.

Tables I and II present the changes in backscatter cross section that occur for Case 2.4 and 2.5, respectively, in the 110 ms prior to incipient jet formation. For Case 2.4, this interval extends from wave 3 to wave 12. For Case 2.5, the interval goes from waves 3 to 7. Tables I and II show that the change (usually an increase) in backscatter cross section decreases significantly as incidence angle decreases.

If the radar views wave 16 of Case 2.4 and wave 7 of Case 2.5 from the backside of the wave, $\theta = -85°$, for example, the backscatter cross sections are reduced significantly; for wave 16 of Case 2.4

$$\sigma_{\mathrm{HH}} = 1.0 \times 10^{-5}\,\mathrm{m}^2 \quad (7.0\,\mathrm{m}^2) \tag{5}$$

$$\sigma_{\mathrm{VV}} = 3.0 \times 10^{-3}\,\mathrm{m}^2 \quad (0.21\,\mathrm{m}^2) \tag{6}$$

and for wave 7 of Case 2.5,

$$\sigma_{\mathrm{HH}} = 2.9 \times 10^{-6}\ \mathrm{m}^2 \quad (57\,\mathrm{m}^2) \tag{7}$$

$$\sigma_{\mathrm{VV}} = 3.6 \times 10^{-3}\ \mathrm{m}^2 \quad (0.77\,\mathrm{m}^2) \tag{8}$$

where the value in parentheses are the $\theta = +85°$ values that appear in Figs. 3 and 4.

To see if the $\theta = 85°$ backscatter cross sections of breaking waves fit any simple models, we will calculate σ_{HH} and σ_{VV} for a series of scaled waves, which will determine the dependence of cross section on the scaling factor. This dependence will then be compared with that of simple models. As explained in Section II, these scaling calculations will also provide an estimate of backscatter cross section for waves of different height that are at the same stage of the breaking process apart from the effects of surface tension. Specifically,

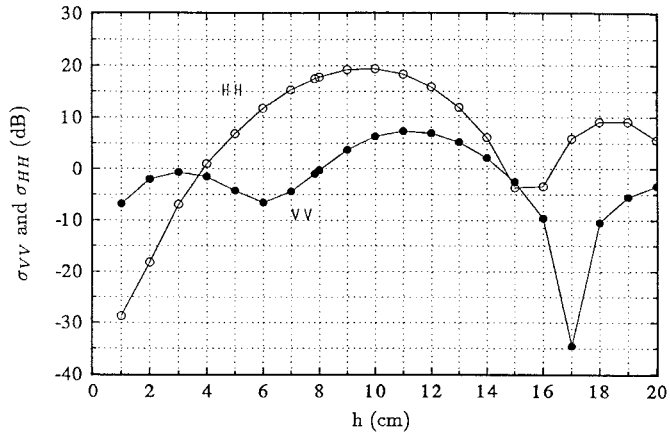

Fig. 9. $\sigma_{\rm HH}$ and $\sigma_{\rm VV}$ for a scaled wave 7 of Case 2.5.

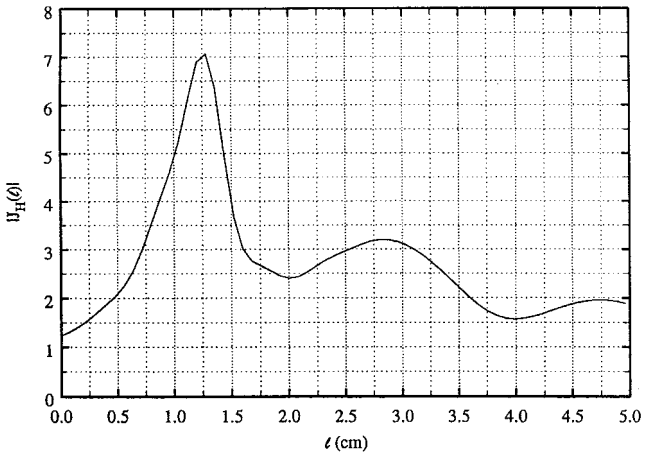

Fig. 10. $J_H(\ell)$ versus ℓ for wave 7 and slope-modified waves.

we use the formula

$$z = \eta(y;h) = hf\left(\frac{y}{h}\right) \tag{9}$$

to produce a series of scaled waves of the same shape but different crest heights; h is the crest height above $z = 0$ so that the maximum value of f is one. Note that (9) does not change the slope of η, only its length scale. Our series of scaled waves will be derived from wave 7 of Case 2.5 because that wave produces the largest $\sigma_{\rm HH}$ of any of the waves in Figs. 3 and 4; for wave 7, $h = 7.854$ cm. Fig. 9 shows the scaled results for h varying from 1 to 20 cm. The backscatter dependence of $\sigma_{\rm HH}$ or $\sigma_{\rm VV}$ obeys no simple model, such as the h^2 dependence of scattering by a flat plate or the h dependence of scattering by a singly curved surface. Furthermore, no simple interference model we have examined agrees with the h dependence of Fig. 9, for both $\sigma_{\rm HH}$ and $\sigma_{\rm VV}$, although the maximum in $\sigma_{\rm HH}$ (at $h \cong 10$ cm) does occur near the value predicted by simple X-band constructive interference from a direct ray and a reflected ray above a plane surface

$$h = \frac{\lambda}{4\cos\theta} = 8.6 \text{ cm} \tag{10}$$

where $\lambda = 3$ cm, $\theta = 85°$. Fig. 9 also shows that the backscatter from wave 7 is, with ϵ fixed at $65 + i40$, highly dispersive.

As was previously noted [5], multiple scattering effects dominate the H-pol $\theta = 85°$ backscatter from wave 7, Case 2.5. For this wave (at $\theta = 85°$), the tangent plane approximation to the imperfect conductor equations (with geometrical optics shadowing) results in

$$\sigma_{\rm HH}^{\rm TP} = 2.0\,{\rm m}^2 \quad (57\,{\rm m}^2) \tag{11}$$

and

$$\sigma_{\rm VV}^{\rm TP} = 1.8\,{\rm m}^2 \quad (0.77\,{\rm m}^2) \tag{12}$$

where the values in the parantheses are the computed values from Fig. 4. Note that the actual value of $\sigma_{\rm HH}$ is 15 dB larger than the tangent plane value, which shows the importance of multiple scattering, while the actual value of $\sigma_{\rm VV}$ is only 4 dB below the tangent plane value.

The electromagnetic surface current $J_H(\ell)$ for wave 7 of Case 2.5, which is shown in Fig. 10, has a sharp peak at $\ell = 12.8$ mm. Examination of the wave form for this case shows that the peak in the current is located close to the front of the incipient jet. This position may explain the result of Trizna *et al.* [10] that large H-pol sea spikes at low-grazing angles can be located near the crests of steepening waves, a conclusion drawn from X-band backscatter experiments on paddle-generated waves in a tank.

V. Summary and Conclusions

By calculating the X-band backscatter from two temporal series (1- and 2.3-m wavelength) of simulated (and idealized!) sea waves that are steepening and undergoing breaking, we have shown that:

1) the backscatter for both H-pol and V-pol has the characteristic of a sea spike at an 85° incidence (5° grazing) angles;
2) for incidence angles of 60° and 40° sea-spike behavior is exhibited only for Case 2.5 (1 m) at 60°; the variation with time of the backscatter cross sections for Case 2.4 (2.3 m) at 60° and for both cases at 40° is too slow to be described as a sea spike;
3) a smaller amplitude steepening sea wave can produce a larger sea spike than a steepening sea wave with a significantly greater height;
4) a sea spike can be produced by a steepening wave before a noticeable jet begins to form at the crest of the wave;
5) in H-pol, a sharply peaked electromagnetic current occurs near the crests of the steepening waves, which is consistent with the observations of Trizna *et al.* [10] that H-pol sea spikes originate near the crests of waves;
6) no simple scattering model we have examined explains the origin of sea spikes; perpendicularity just forward of a crest and for H-pol, constructive interference at the crest region between the directly incident electromagnetic wave and the electromagnetic wave reflected from the surface ahead of the sea wave appear to be important factors that need to be present.

REFERENCES

[1] L. B. Wetzel, "Sea clutter," in *Radar Handbook*, M. I. Skolnik, Ed., 2nd ed. New York: McGraw-Hill, 1990, ch. 13.

[2] C. A. Jensen, J. F. Vesecky, and R. E. Glazman, "Diffraction from sharply peaked waves as an ocean surface scattering mechanism," *IGARSS '92*, 1992, vol. II, pp. 1771–1773.

[3] D. Holliday, L. L. DeRaad, Jr., and G. J. St-Cyr, "Wedge scattering by the method of iteration," *IEEE Trans. Geosci. Remote Sensing*, vol. GRS-33, pp. 449–456, Mar. 1995.

[4] ———, "Forward–backward: A new method for computing low-grazing angle scattering," *IEEE Trans. Antennas Propagat.*, vol. 44, pp. 722–729, May 1996.

[5] ———, "Forward–backward method for scattering from imperfect conductors," *IEEE Trans. Ant. Propag.*, to be published.

[6] P. Wang, Y. Yao, and M. P. Tulin, "An efficient numerical tank for nonlinear water waves, based on the multi-subdomain approach with B.E.M.," *Int. J. Num. Math. Fluids*, vol. 20, pp. 1315–1336, 1995.

[7] Y. Yao, private communications, Nov. and Dec. 1995.

[8] J. A. Saxton, "Electrical properties of water: Reflection characteristics of water surfaces at V.H.F.," *Wireless Engineer*, pp. 288–292, Sept. 1949.

[9] E. F. Knott, "Radar cross section," in *Radar Handbook*, M. I. Skolnik, Ed., 2nd ed., New York: McGraw-Hill, 1990, ch. 11.

[10] D. B. Trizna, J. P. Hansen, P. Hwang, and J. Wu, "Laboratory studies of radar sea spikes at low grazing angles," *J. Geophys. Res.*, vol. 96, pp. 12 529–12 537, 1991.

Dennis Holliday, for photograph and biography, see p. 107 of this issue.

Lester L. DeRaad, Jr., for photograph and biography, see p. 107 of this issue.

Gaetan J. St-Cyr, for photograph and biography, see p. 107 of this issue.